MITSUBISHI ELECTRIC RESEARCH LABORATORIES
https://www.merl.com

A Real-time High C-rate Lithium-ion Battery Fast Charging Strategy

Lu, Zehui; Tu, Hao; Fang, Huazhen; Wang, Yebin; Mou, Shaoshuai

TR2025-127 August 26, 2025

Abstract

This article investigates real-time fast charging for lithium-ion batteries at high C-rates. First, an electrochemical- thermal-inspired battery model is presented to capture key dynamics accurately. The model is validated through hardware experiments, showing small modeling errors across a wide range of charging (up to 4 C) and discharging (up to 14.5 C) currents. A fast-charging framework is then proposed, consisting of two components: an offline trajectory optimization and an online current reshaping algorithm. First, the offline component solves a time-optimal charging trajectory optimization problem once at the start of the charging process. This generates an optimal reference trajectory for battery states and controls, which is then used by the online component. Second, the online component continually reshapes the reference charging current in real time. Operating at a higher frequency, it adjusts the current based on the present state and the reference current for the next time instance, ensuring compliance with charging constraints. Numerical experiments confirm the effectiveness and computational efficiency of the proposed framework.

IEEE Conference on Control Technology and Applications (CCTA) 2025

Mitsubishi Electric Research Laboratories, Inc.
201 Broadway, Cambridge, Massachusetts 02139

A Real-time High C-rate Lithium-ion Battery Fast Charging Strategy

Zehui Lu, Hao Tu, Huazhen Fang, Yebin Wang, Shaoshuai Mou

***Abstract*— This article investigates real-time fast charging for lithium-ion batteries at high C-rates. First, an electrochemical-thermal-inspired battery model is presented to capture key dynamics accurately. The model is validated through hardware experiments, showing small modeling errors across a wide range of charging (up to 4 C) and discharging (up to 14.5 C) currents. A fast-charging framework is then proposed, consisting of two components: an offline trajectory optimization and an online current reshaping algorithm. First, the offline component solves a time-optimal charging trajectory optimization problem once at the start of the charging process. This generates an optimal reference trajectory for battery states and controls, which is then used by the online component. Second, the online component continually reshapes the reference charging current in real time. Operating at a higher frequency, it adjusts the current based on the present state and the reference current for the next time instance, ensuring compliance with charging constraints. Numerical experiments confirm the effectiveness and computational efficiency of the proposed framework.**

I. Introduction

Lithium-ion batteries (LiBs) have become essential across various sectors, including electric vehicles (EVs) [1] and electric vertical takeoff and landing (eVTOL) aircraft [2]. These applications require fast charging and high output power, which in turn demand high charging/discharging currents. For example, compared to EVs, eVTOL aircraft require batteries capable of discharging at rates three times higher during takeoff and landing, with charging frequencies up to four times faster [2]. However, fast charging LiBs at high C-rates poses significant challenges due to the excessive heat generated by high currents, potentially jeopardizing both battery safety and lifespan. Ensuring safe and efficient fast charging requires accurate modeling of battery dynamics, including electrical, thermal, and chemical behaviors under high C-rate conditions. Two primary categories of LiB models have emerged: Electrochemical Models and Equivalent Circuit Models (ECMs).

Electrochemical models offer high modeling fidelity but tend to be computationally intensive. For onboard applications, where fast computation is essential, models that balance accuracy and efficiency are highly desirable. One popular choice is the pseudo-2D Doyle–Fuller–Newman (DFN) model, which describes lithium-ion (Li-ion) diffusion and charge transfer within a cell's electrodes, electrolyte, and separator [3]. A more computationally efficient alternative is the single-particle model (SPM), which simplifies each electrode as a single spherical particle, neglecting electrolyte dynamics [4]. While this enhances computational speed, the SPM is typically limited to low C-rates (no higher than 1 C) [5]. In contrast, ECMs, incorporating circuit components, provide a computationally efficient way of representing the dynamics of LiB's key characteristics from the user's perspective, including state of charge (SoC), voltage, temperature, and power capabilities during charging and discharging. ECMs are easy to interpret, simple to calibrate, and scalable for larger battery systems. Their low-order ordinary differential equations (ODEs) allow for fast onboard computation, making ECMs a popular choice for battery management systems with limited computing resources.

Recent literature has explored advanced real-time battery charging control techniques. For example, a two-level architecture is proposed in [6]–[8], using a simplified linear dynamic model derived from DFN. This architecture employs a low-level linear quadratic regulator to ensure stability and fast reference tracking, while a high-level reference governor enforces constraint satisfaction by adjusting the reference. Feng et al. [9] apply cascade-CBF (control barrier function) to modify the conventional constant current/constant voltage (CC/CV) strategy, using the thermal-ECM model proposed in [10]. Based on a DFN model, Li et al. [11] converts a constrained optimal control problem into an output tracking problem through nonlinear model inversion-based control, thereby improving real-time computation performance. Meanwhile, researchers have explored bridging the gap between ECMs and electrochemical models. The nonlinear double capacitor (NDC) model [5], for instance, approximates Li-ion diffusion within the electrodes and captures nonlinear voltage behavior, offering a reduced-order circuit analog to the SPM. A variant, the thermal-NDC model [12], integrates a two-state lumped thermal model [10] to account for temperature-dependent electrothermal dynamics during charging at up to 1.5 C.

Despite their widespread use, the simplicity of ECMs limits their accuracy, especially at high C-rates [13]. One of the more advanced ECMs, the BattX model [13], builds upon the Single-Particle Model with Electrolyte and Thermal dynamics (SPMeT) [14]–[16]. It employs equivalent circuits to simulate a LiB cell's electrode, electrolyte, and thermal dynamics independently, which are then combined into a comprehensive ECM. This approach improves model accuracy across a wide range of C-rates while maintaining

Z. Lu and S. Mou are with the School of Aeronautics and Astronautics, Purdue University, West Lafayette, IN 47907, USA {lu846,mous}@purdue.edu

H. Tu and H. Fang are with the Department of Mechanical Engineering, University of Kansas, Lawrence, KS 66045, USA {tuhao,fang}@ku.edu

Y. Wang is with Mitsubishi Electric Research Laboratories, Cambridge, MA 02139, USA yebinwang@ieee.org

computational efficiency, making it suitable for real-time fast charging. However, the increased state dimension of the BattX model, at least 10 states compared to the 4-state thermal-NDC model in [12], introduces a computational challenge. These challenges become especially significant when managing a large number of battery cells or implementing long-horizon model predictive control (MPC), primarily due to the curse of dimensionality. Thus, designing an efficient real-time fast charging strategy for high-fidelity battery models remains a significant challenge.

A. Problem Statement, Summary & Contributions

The problem of interest is to develop a real-time fast-charging strategy for LiBs in high C-rate scenarios. To tackle this, an electrochemical-thermal-inspired battery model is used to accurately capture critical dynamic processes, including electrode-phase diffusion, electrolyte-phase diffusion, thermal behavior, and voltage response. The model is validated through hardware experiments, demonstrating small modeling errors across a wide range of charging (up to 4 C) and discharging (up to 14.5 C) currents.

Building on this, a real-time fast-charging framework is introduced, comprising two components: (1) an offline trajectory optimization and (2) an online current reshaping algorithm. The offline component formulates a time-optimal charging trajectory problem using coarse time discretization. This problem is solved once at the start of the charging process to generate a reference trajectory for battery states and control variables. This reference trajectory is then provided to the online component. The online current reshaping algorithm operates at a higher frequency, continually adjusting the charging current in real time based on the present state and reference point at the next time instance. By employing a computationally efficient one-step prediction method, the reshaping algorithm ensures compliance with charging constraints while refining the initial reference trajectory. Numerical experiments and comparisons validate the proposed framework's effectiveness in maintaining charging constraints throughout the process.

The primary contributions of this work are as follows.

1) Real-Time Fast-Charging Framework: A computationally efficient fast-charging strategy is introduced, combining offline trajectory optimization with real-time current reshaping. Numerical results confirm the framework's effectiveness in safely and efficiently achieving fast charging.

2) Model Validation: This article utilizes a modified electrochemical-thermal-inspired model, based on the BattX model [13]. This model is validated through hardware experiments with a wide current range, demonstrating its ability to accurately capture battery dynamics with the identified model parameters.

Notations. The real number set and natural number set are denoted by $\mathbb{R}$ and $\mathbb{N}$, respectively. Let $[\![a, b]\!]$ denote a set of all integers between $a \in \mathbb{Z}$ and $b \in \mathbb{Z}$, with both ends included. For $\boldsymbol{x}, \boldsymbol{y} \in \mathbb{R}^n$, $\boldsymbol{x} \leq \boldsymbol{y}$ indicates element-wise inequality. Denote column stack as $\text{col}\{\boldsymbol{v}_1, \cdots, \boldsymbol{v}_a\} \triangleq \begin{bmatrix}\boldsymbol{v}_1{}^\top & \cdots & \boldsymbol{v}_a{}^\top\end{bmatrix}^\top$. For a vector $\boldsymbol{x} \in \mathbb{R}^n$, $\boldsymbol{x}[-1] \in \mathbb{R}$ indicates the last element of $\boldsymbol{x}$. Let $\mathbf{0}_n, \mathbf{1}_n \in \mathbb{R}^n$ denote a zero and a one vector.

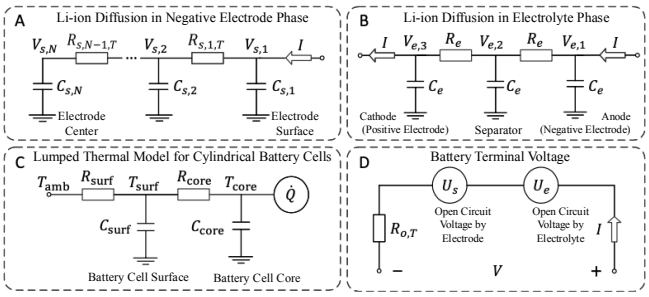

Fig. 1. The modified BattX battery model proposed in this article.

II. System Dynamics, Parameters & Constraints

This section introduces a modified electrochemical-thermal-inspired battery model, based on the BattX model [13]. The proposed model characterizes the key dynamic processes occurring in a LiB cell across a broad range of current rates. As illustrated in Fig. 1, the model adopts a similar philosophy to ECMs and is represented by four coupled sub-circuits, labeled A through D. These sub-circuits conceptually correspond to the cell's distinct dynamics respectively: electrode-phase lithium-ion (Li-ion) diffusion, electrolyte-phase Li-ion diffusion, thermal dynamics, and voltage response. Note that the sub-circuits are conceptual representations and do not correspond directly to physical components within the battery cell.

A. System Dynamics

Sub-circuit A uses a chain of $N \in \mathbb{N}$ $(N \geq 3)$ resistors and capacitors to approximate the Li-ion diffusion in the negative electrode (solid) phase, i.e., $\forall i \in [\![2, N-1]\!]$,

$$\dot{V}_{\mathrm{s},1}(t) = \frac{V_{\mathrm{s},2}(t) - V_{\mathrm{s},1}(t)}{C_{\mathrm{s},1} R_{\mathrm{s},1,\mathrm{T}}(t)} + \frac{I(t)}{C_{\mathrm{s},1}}, \tag{1a}$$

$$\dot{V}_{\mathrm{s},i}(t) = \frac{V_{\mathrm{s},i-1}(t) - V_{\mathrm{s},i}(t)}{C_{\mathrm{s},i} R_{\mathrm{s},i-1,\mathrm{T}}(t)} + \frac{V_{\mathrm{s},i+1}(t) - V_{\mathrm{s},i}(t)}{C_{\mathrm{s},i} R_{\mathrm{s},i,\mathrm{T}}(t)}, \tag{1b}$$

$$\dot{V}_{\mathrm{s},N}(t) = \frac{V_{\mathrm{s},N-1}(t) - V_{\mathrm{s},N}(t)}{C_{\mathrm{s},N} R_{\mathrm{s},N-1,\mathrm{T}}(t)}, \tag{1c}$$

where $I(t)$ is the current at time t, with $I > 0$ for charging and $I < 0$ for discharging. For all $i \in [\![1, N]\!]$, $V_{\mathrm{s},i}(t)$, $i = 1, \cdots, N$, are the voltages across the capacitors $C_{\mathrm{s},i}$, which correspond to the normalized Li-ion concentrations at N different locations of an electrode, from the surface to the center, that spread along the radius of the electrode sphere. $C_{\mathrm{s},i}$ are analogous to the volumes of the subdomains if one subdivides the electrode sphere at these discrete locations. $R_{\mathrm{s},i,\mathrm{T}}(t)$ represent charge transfer resistance, which are temperature-dependent (state-dependent) and introduced

later. The positive electrode dynamics are not considered due to the charge conservation assumption between the positive and negative electrodes.

Sub-circuit B uses a chain of 3 resistors and capacitors to approximate the Li-ion diffusion in the electrolyte,

$$\dot{V}_{\mathrm{e},1}(t) = \frac{V_{\mathrm{e},2}(t) - V_{\mathrm{e},1}(t)}{C_{\mathrm{e}}R_{\mathrm{e}}} + \frac{I(t)}{C_{\mathrm{e}}}, \tag{2a}$$

$$\dot{V}_{\mathrm{e},2}(t) = \frac{V_{\mathrm{e},1}(t) - 2V_{\mathrm{e},2}(t) + V_{\mathrm{e},3}(t)}{C_{\mathrm{e}}R_{\mathrm{e}}}, \tag{2b}$$

$$\dot{V}_{\mathrm{e},3}(t) = \frac{V_{\mathrm{e},2}(t) - V_{\mathrm{e},3}(t)}{C_{\mathrm{e}}R_{\mathrm{e}}} - \frac{I(t)}{C_{\mathrm{e}}}. \tag{2c}$$

Sub-circuit B is analogous to the one-dimensional electrolyte-phase diffusion that is discretized along the spatial coordinate. $V_{\mathrm{e},j}(t)$, $j = 1,2,3$, indicate the normalized Li-ion concentrations at the anode, separator, and cathode, respectively. R_{e} represents resistance to the diffusion. The spatial discretization is assumed to be uniform in the electrolyte, thus leading to the same values of C_{e} and R_{e} for each region.

Remark 1. *Since $V_{\mathrm{s},i}$ and $V_{\mathrm{e},j}$ are the normalized Li-ion concentrations at different locations and a LiB cell has a capacity limit, $V_{\mathrm{s},i}$ and $V_{\mathrm{e},j}$ must have an upper and lower bound. $\overline{V}_{\mathrm{s}} = 1$ V and $\underline{V}_{\mathrm{s}} = 0$ V are the upper and lower bound for $V_{\mathrm{s},i}(t)$, $\forall i \in [\![1, N]\!]$. $\overline{V}_{\mathrm{e}} = 1$ V and $\underline{V}_{\mathrm{e}} = 0$ V are the upper and lower bound for $V_{\mathrm{e},j}(t)$, $\forall j = 1,2,3$. Thus, sub-circuit B assumes that a LiB cell is at equilibrium when $V_{\mathrm{e},j}(t) = 0.5$ V, $\forall j = 1,2,3$. Note that $\sum_{i=1}^{N} C_{\mathrm{s},i}\overline{V}_{\mathrm{s}}$ indicates the cell total capacity, and $\sum_{i=1}^{N} C_{\mathrm{s},i}V_{\mathrm{s},i}(t)$ indicates the battery's remaining capacity.*

Define the SoC as the (unitless) percentage of the currently available charge over the total charge capacity:

$$\mathrm{SoC}(t) \triangleq \frac{\sum_{i=1}^{N} C_{\mathrm{s},i}V_{\mathrm{s},i}(t)}{\sum_{i=1}^{N} C_{\mathrm{s},i}\overline{V}_{\mathrm{s}}} \times 100\%. \tag{3}$$

This article formulates a minimal state-space representation for the battery dynamics, thus SoC is not a system state but acts as another coordinate of the states $V_{\mathrm{s},i}$.

Sub-circuit C is a lumped circuit model for the thermal dynamics of the cylindrical LiB cell, with the design inspired by [10]. The dynamics are given by

$$\dot{T}_{\mathrm{core}}(t) = \frac{\dot{Q}(t)}{C_{\mathrm{core}}} + \frac{T_{\mathrm{surf}}(t) - T_{\mathrm{core}}(t)}{R_{\mathrm{core}}C_{\mathrm{core}}}, \tag{4a}$$

$$\dot{T}_{\mathrm{surf}}(t) = \frac{T_{\mathrm{amb}} - T_{\mathrm{surf}}(t)}{R_{\mathrm{surf}}C_{\mathrm{surf}}} - \frac{T_{\mathrm{surf}}(t) - T_{\mathrm{core}}(t)}{R_{\mathrm{core}}C_{\mathrm{surf}}}, \tag{4b}$$

where T_{amb} is the ambient temperature; $T_{\mathrm{surf}}(t)$ and $T_{\mathrm{core}}(t)$ are the cell surface and core temperature, respectively; C_{surf}, C_{core} and R_{surf}, R_{core} represent the thermal capacitance and resistance at the surface and core, respectively. $\dot{Q}(t)$ is the internal heat generation rate accompanying electrochemical reactions inside the cell during charging/discharging, i.e.

$$\dot{Q}(t) = I(t)(V(t) - U_{\mathrm{s}}(\mathrm{SoC}(t))) + I(t)T_{\mathrm{core}}(t)\frac{dU_{\mathrm{s}}}{dT_{\mathrm{core}}}, \tag{5}$$

where $V(t)$ is the cell's terminal voltage provided by sub-circuit D, $U_{\mathrm{s}}(\mathrm{SoC}(t))$ is the open-circuit voltage (OCV) function, which is given by sub-circuit D. The term $I(t)(V(t) - U_{\mathrm{s}}(\mathrm{SoC}(t)))$ considers the irreversible heat generation from ohmic loss. Unlike the BattX model [13], this article accounts for reversible entropic heating, i.e., $I(t)T_{\mathrm{core}}(t)\frac{dU_{\mathrm{s}}}{dT_{\mathrm{core}}}$, which becomes significant in high C-rate scenarios. The entropic coefficient is assumed to be a function of SoC [17]:

$$\frac{dU_{\mathrm{s}}}{dT_{\mathrm{core}}} = c_1 + c_2\mathrm{SoC}(t) + c_3\mathrm{SoC}(t)^2, \tag{6}$$

where c_1, c_2, c_3 are constant coefficients.

Finally, sub-circuit D summarizes the effects of the solid and electrolyte phase dynamics on the terminal voltage $V(t)$,

$$V(t) = U_{\mathrm{s}}(V_{\mathrm{s},1}(t)) + U_{\mathrm{e}}(V_{\mathrm{e},1}(t), V_{\mathrm{e},3}(t)) + R_{\mathrm{o,T}}(t)I(t), \tag{7}$$

where the first and second terms account for the open circuit voltage in the electrode phase and the voltage caused by the electrolyte phase dynamics, respectively; the third term captures a voltage due to film resistance and over-potential. The OCV mapping $U_{\mathrm{s}} : \mathbb{R} \to \mathbb{R}$ is

$$U_{\mathrm{s}}(V_{\mathrm{s},1}) = \frac{\alpha_0 V_{\mathrm{s},1}^2 + \alpha_1 V_{\mathrm{s},1} + \alpha_2 \underline{V}}{V_{\mathrm{s},1}^3 + \alpha_3 V_{\mathrm{s},1}^2 + \alpha_4 V_{\mathrm{s},1} + \alpha_2}, \tag{8}$$

where $\alpha_i, i = [\![0, 4]\!]$ are constant coefficients; $\underline{V} > 0$ V is a constant minimum terminal voltage. In the electrochemical model SPMeT, the electrolyte potential depends on the electrolyte concentration at the anode and cathode. Thus, U_{e} is a function of $V_{\mathrm{e},1}$ and $V_{\mathrm{e},3}$, i.e.

$$U_{\mathrm{e}}\left(V_{\mathrm{e},1}(t), V_{\mathrm{e},3}(t)\right) = \beta_1 \cdot \ln\left(\frac{V_{\mathrm{e},1}(t) + \beta_2}{V_{\mathrm{e},3}(t) + \beta_2}\right), \tag{9}$$

where $\beta_i, i = 1,2$ are constant coefficients. $R_{\mathrm{o,T}}(t)$ is an internal resistance dependent on SoC and $T_{\mathrm{core}}(t)$, capturing film resistance and over-potential,

$$R_{\mathrm{o,T}}(t) = R_{\mathrm{o}}(\mathrm{SoC}(t)) \cdot \exp\left(\kappa_1\left(\frac{1}{T_{\mathrm{core}}(t)} - \frac{1}{T_{\mathrm{ref}}}\right)\right), \tag{10}$$

where κ_1 is a constant coefficient, T_{ref} is a constant reference temperature of the Arrhenius-like equation. $R_{\mathrm{o}}(\mathrm{SoC}(t))$ captures the dependency of $R_{\mathrm{o,T}}$ on SoC:

$$R_{\mathrm{o}}(\mathrm{SoC}(t)) = \gamma_1 + \gamma_2\mathrm{SoC}(t) + \gamma_3\mathrm{SoC}(t)^2, \tag{11}$$

where $\gamma_1, \gamma_2, \gamma_3$ are coefficients. Rather than the monotonically decreasing exponential function employed in the BattX model [13], this article utilizes the quadratic function (11) to achieve greater modeling accuracy in high C-rate scenarios. An Arrhenius relationship can be used to capture the relation between the electrode-phase diffusion resistances $R_{\mathrm{s,1,T}}(t)$ and temperature:

$$R_{\mathrm{s,1,T}}(t) = R_{\mathrm{s,1}} \cdot \exp\left(\kappa_2\left(\frac{1}{T_{\mathrm{core}}(t)} - \frac{1}{T_{\mathrm{ref}}}\right)\right). \tag{12}$$

TABLE I

BATTERY PARAMETERS

Parameter	Value	Parameter	Value
$C_{\mathrm{s},1}$	4840.181 F	$R_{\mathrm{s},1}$	0.086 Ω
C_{e}	9171.013 F	R_{e}	0.025 Ω
C_{core}	46.064 J/K	R_{core}	1.299 K/W
C_{surf}	30.743 J/K	R_{surf}	6.967 K/W
κ_1	2829.399 K	κ_2	2415.149 K
β_1	5.404 V	β_2	30.428 V
c_1	-0.00048 V/K	c_2	0.00159 V/K
c_3	-0.00108 V/K	α_0	-180.557 V^2
α_1	179.899 V^3	α_2	0.614 V^3
α_3	-55.834 V	α_4	54.427 V^2
γ_1	0.050 Ω	γ_2	-0.059 Ω
γ_3	0.039 Ω	σ_2	1.77
σ_3	4.00	σ_4	15.98
η_2	0.6066	η_3	0.3115
η_4	0.1148	η_5	0.0164
T_{ref}	298.15 K	N	5

Due to the spatial discretization, $R_{\mathrm{s},i}(t), i \in [\![2, N-1]\!]$ and $C_{\mathrm{s},j}, j \in [\![2, N]\!]$ have the following relationships to $R_{\mathrm{s},1,\mathrm{T}}(t)$ and $C_{\mathrm{s},1}$ respectively [13],

$$R_{\mathrm{s},i,\mathrm{T}}(t) = \sigma_i R_{\mathrm{s},1,\mathrm{T}}(t), \ \forall i \in [\![2, N-1]\!], \tag{13a}$$

$$C_{\mathrm{s},j} = \eta_j C_{\mathrm{s},1}, \ \forall j \in [\![2, N]\!], \tag{13b}$$

where $\sigma_i, i \in [\![2, N-1]\!]$ and $\eta_j, j \in [\![2, N]\!]$ are predefined constant coefficients.

The continuous-time system dynamics are given by (1), (2), (4) - (13). However, the system dynamics are not control-affine due to the term $I^2(t)$ in $I(t)V(t)$ of (5), together with the definition of $V(t)$ in (7). And one system output $V(t)$ is not solely determined by the states. To address these, the current $I(t)$ can be modeled as an additional state with the following fictitious dynamics,

$$\dot{I}(t) = u_{\mathrm{f}}(t), \tag{14}$$

where $u_{\mathrm{f}}(t) \in \mathbb{R}$ is a fictitious control input. Thus, denote the augmented system state as $\boldsymbol{x} \triangleq \mathrm{col}\{V_{\mathrm{s},1}, \cdots, V_{\mathrm{s},N}, V_{\mathrm{e},1}, V_{\mathrm{e},2}, V_{\mathrm{e},3}, T_{\mathrm{core}}, T_{\mathrm{surf}}, I\} \in \mathbb{R}^n$ ($n \triangleq N+6$), the fictitious system control as $\boldsymbol{u} \triangleq u_{\mathrm{f}} \in \mathbb{R}$, the augmented system output as $\boldsymbol{y} \triangleq \mathrm{col}\{T_{\mathrm{surf}}, I, V\} \in \mathbb{R}^3$. Given (1), (2), (4) - (13), the continuous-time system dynamics are

$$\dot{\boldsymbol{x}}(t) = \boldsymbol{f}_{\mathrm{c}}(\boldsymbol{x}, \boldsymbol{u}) = \boldsymbol{f}(\boldsymbol{x}) + \boldsymbol{g}(\boldsymbol{x})\boldsymbol{u}, \tag{15}$$

where $\boldsymbol{f}_{\mathrm{c}} : \mathbb{R}^n \times \mathbb{R} \mapsto \mathbb{R}^n$, $\boldsymbol{f} : \mathbb{R}^n \mapsto \mathbb{R}^n$, $\boldsymbol{g} : \mathbb{R}^n \mapsto \mathbb{R}^n$; $\boldsymbol{g}(\boldsymbol{x}) = \mathrm{col}\{\boldsymbol{0}_{N+5}, 1\}$, $\boldsymbol{f}(\boldsymbol{x}) = \boldsymbol{f}_{\mathrm{c}}(\boldsymbol{x}, \boldsymbol{u}) - \boldsymbol{g}(\boldsymbol{x})\boldsymbol{u}$. According to (7), the terminal voltage $V(t)$ can be determined given the state $\boldsymbol{x}(t)$, denoted as $V = g_{\mathrm{V}}(\boldsymbol{x})$ with $g_{\mathrm{V}} : \mathbb{R}^n \mapsto \mathbb{R}$. Similarly, according to (3), denote $\mathrm{SoC} = g_{\mathrm{s}}(\boldsymbol{x})$ with $g_{\mathrm{s}} : \mathbb{R}^n \mapsto \mathbb{R}$. Note that the actual outputs of a battery cell are terminal voltage $V(t)$ and surface temperature $T_{\mathrm{surf}}(t)$.

B. Parameter Identification and Model Validation

Using the parameter identification method proposed in [13], the necessary parameters for the battery dynamics (15) are identified and summarized in Table I, based on an A123 ANR26650M1B LFP (LiFePO4) cell. The cell's nominal capacity is 2.5 Ah, and its 1 C current is 2.5 A. The maximum charging current is $\overline{I} = 10$ A (4 C). The maximum and minimum terminal voltages are $\overline{V} = 3.6$ V and $\underline{V} = 2.26$ V, respectively.

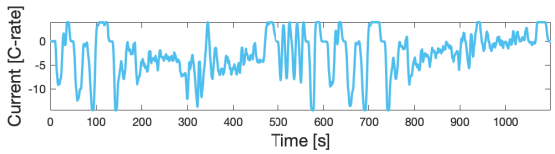

(a) Battery current trajectory given the US06 profile.

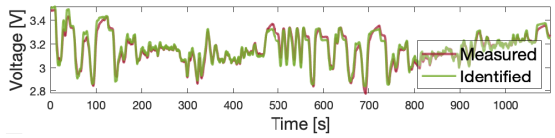

(b) Battery terminal voltage from the experimental and simulation data.

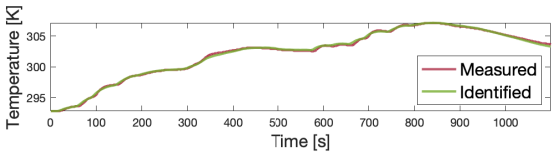

(c) Battery surface temperature from the experimental and simulation data.

Fig. 2. Experimental validation for the proposed model with the identified parameters and the US06 profile.

The obtained model is validated by charging and discharging an A123 ANR26650M1B LFP cell given the US06 current profile with a wide current range $[-14.5, 4]$ C. The experimental data includes measurement trajectories of battery terminal voltage and surface temperature. The simulation data with the same US06 profile is generated by the proposed model and the identified parameters in Table I. Fig. 2 shows the experimental validation of the proposed model under the US06 profile. Fig. 2a shows the battery current trajectory given the US06 profile. Fig. 2b shows the battery terminal voltage trajectories from the experimental data and simulation data. Fig. 2c shows the battery surface temperature trajectories from the experimental data and simulation data. Fig. 3 shows the absolute error trajectories of the battery terminal voltage (Fig. 3a) and surface temperature (Fig. 3b) between measurement and simulation data. The root mean square error (RMSE) for the terminal voltage and surface temperature are 0.0287 V and 0.14 K, respectively.

C. Constraints

This subsection introduces some necessary constraints required for fast charging. To begin with, the SoC must be constrained to avoid overcharging, i.e.

$$\underline{\mathrm{SoC}} \leq \mathrm{SoC}(t) \leq \overline{\mathrm{SoC}}, \ \forall t. \tag{16}$$

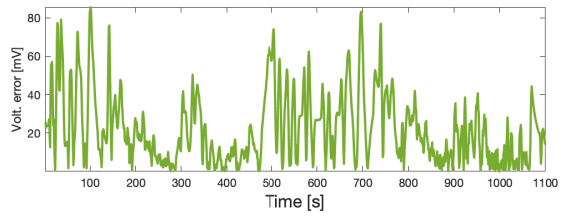

(a) Absolute error between measurement and simulation data of battery terminal voltage.

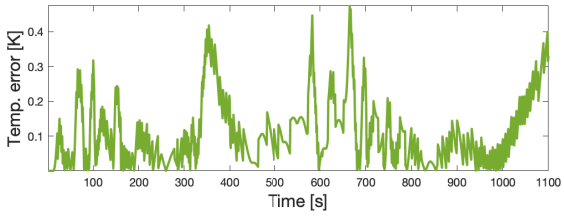

(b) Absolute error between measurement and simulation data of battery surface temperature.

Fig. 3. Absolute error trajectories between measurement and simulation data of battery terminal voltage and surface temperature given the identified parameters and the US06 profile.

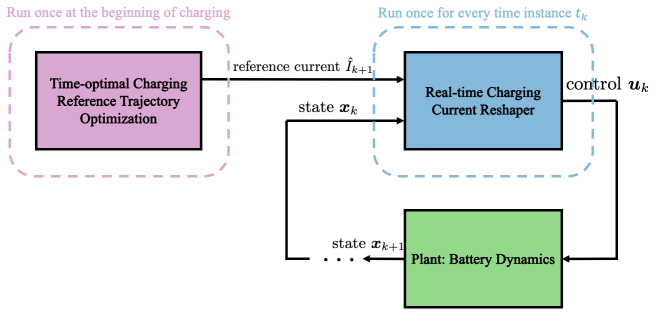

Fig. 4. Proposed framework for real-time high C-rate battery fast charging.

The current, terminal voltage, and temperature must be within limits, i.e. $\forall t$,

$$\underline{I} \le I(t) \le \overline{I},\ \underline{V} \le V(t) \le \overline{V}, \tag{17a}$$
$$\underline{T}_{\rm core} \le T_{\rm core}(t) \le \overline{T}_{\rm core}, \tag{17b}$$
$$\underline{T}_{\rm surf} \le T_{\rm surf}(t) \le \overline{T}_{\rm surf}. \tag{17c}$$

For all capacitors $i \in [\![1, N]\!],\ j = 1, 2, 3,$

$$\underline{V}_{\rm s} \le V_{{\rm s},i}(t) \le \overline{V}_{\rm s},\ \underline{V}_{\rm e} \le V_{{\rm e},j}(t) \le \overline{V}_{\rm e},\ \forall t. \tag{18}$$

III. Methodology

This section proposes a framework for real-time high C-rate fast charging. As summarized in Fig. 4, the proposed framework includes two components, an offline time-optimal charging reference trajectory optimization and a real-time charging current reshaper.

First, as illustrated by the pink block in Fig. 4, a time-optimal trajectory optimization (19) is solved once at the start of the charging process, which is

$$\min_{\substack{\boldsymbol{u}_{0:N_{\rm p}-1}\\ \boldsymbol{x}_{1:N_{\rm p}}, t_{\rm f}, \epsilon_{\rm s}}} \quad t_{\rm f} + w_{\rm s}\epsilon_{\rm s}^2 \tag{19a}$$
$$\text{s.t.} \quad \boldsymbol{x}_{k+1} = \boldsymbol{x}_k + \Delta \boldsymbol{f}_{\rm c}(\boldsymbol{x}_k, \boldsymbol{u}_k), \tag{19b}$$
$$\forall k \in [\![0, N_{\rm p}-1]\!] \text{ with given } \boldsymbol{x}_0, \tag{19c}$$
$$V_k = g_{\rm V}(\boldsymbol{x}_k),\ {\rm SoC}_k = g_{\rm s}(\boldsymbol{x}_k), \tag{19d}$$
$$\text{constraints (16)} - \text{(18)},\ \forall k \in [\![1, N_{\rm p}]\!], \tag{19e}$$
$${\rm SoC}_{N_{\rm p}} - {\rm SoC}_{\rm des} \ge \epsilon_{\rm s}, \tag{19f}$$
$$t_{\rm f} \ge 0,\ \Delta = t_{\rm f}/N_{\rm p},\ \epsilon_{\rm s} \in [0, 0.01], \tag{19g}$$

where $N_{\rm p} \in \mathbb{N}$ is a prescribed number of prediction steps; $t_{\rm f} \ge 0$ is a decision variable for the trajectory final time; $\epsilon_{\rm s} \in [0, 0.01]$ is a relaxation variable that ensures the solvability of the optimization as penalized by a prescribed weight $w_{\rm s} > 0$. $\boldsymbol{x}_{1:N_{\rm p}} \triangleq {\rm col}\{\boldsymbol{x}_1, \cdots, \boldsymbol{x}_{N_{\rm p}}\} \in \mathbb{R}^{nN_{\rm p}}$ includes all the states within the prediction horizon; similarly, $\boldsymbol{u}_{0:N_{\rm p}-1} \triangleq {\rm col}\{\boldsymbol{u}_0, \cdots, \boldsymbol{u}_{N_{\rm p}-1}\} \in \mathbb{R}^{N_{\rm p}}$. V_k and ${\rm SoC}_k$ denote the terminal voltage and SoC level at the k-th step in the prediction horizon $[\![0, N_{\rm p}]\!]$. Constraint (19b) describes the discrete-time dynamics via Euler integration from the continuous-time dynamics (15) with time interval $\Delta = t_{\rm f}/N_{\rm p}$, which is an expression of the decision variable $t_{\rm f}$. Constraint (19f) softens the requirement of reaching the exact desired terminal SoC level ${\rm SoC}_{\rm des} = 98\%$. Denote the optimal solution of optimization (19) as $\hat{\boldsymbol{x}}_{1:N_{\rm p}}$, $\hat{\boldsymbol{u}}_{0:N_{\rm p}-1}$, $\hat{t}_{\rm f}$, and $\hat{\epsilon}_{\rm s}$. Then the optimal reference state and control trajectory $\hat{\boldsymbol{x}}_{1:N_{\rm p}}$ and $\hat{\boldsymbol{u}}_{0:N_{\rm p}-1}$ are passed to the second component, i.e. the real-time charging current reshaper.

Second, as demonstrated by the blue block in Fig. 4, at each time instance k, a real-time charging current reshaper takes in the optimal reference current $\hat{I}_{k+1} \equiv \hat{\boldsymbol{x}}_{k+1}[-1]$ at the next time $k+1$ and the present state $\boldsymbol{x}_k$, and reshapes the reference control $\hat{\boldsymbol{u}}_k$ such that the current at next time instance $k+1$ stays as close as possible to the reference value $\hat{I}_{k+1}$, subject to some constraints. Specifically, at each time instance k, given $\hat{I}_{k+1}$, $\boldsymbol{x}_k$, $T_{\rm amb}$, and the reshaper's time interval $\Delta_{\rm p}$, the charging current reshaper is

$$\min_{\boldsymbol{u}_k} \quad ||I_{k+1} - \hat{I}_{k+1}||_2^2 \tag{20a}$$
$$\text{s.t.} \quad I_{k+1} = I_k + \Delta_{\rm p}\boldsymbol{u}_k,\ I_k = \boldsymbol{x}_k[-1], \tag{20b}$$
$$\overline{I} - I_{k+1} \ge 0,\ I_{k+1} - 0 \ge 0, \tag{20c}$$
$$\boldsymbol{x}_{k+1} = \boldsymbol{x}_k + \Delta_{\rm p}\boldsymbol{f}_{\rm c}(\boldsymbol{x}_k, \boldsymbol{u}_k), \tag{20d}$$
$$V_{k+1} \triangleq g_{\rm V}(\boldsymbol{x}_{k+1}) \le \overline{V}. \tag{20e}$$

Constraint (20e) is enforced at the next step, as this constraint is more prone to violation due to its definition (7) and the thermal dynamics (4) - (13). This statement will be validated by the numerical results presented later.

Algorithm 1 summarizes the proposed real-time fast-charging framework. As shown by Line 3, the system state is observed with a smaller sampling time $\Delta_{\rm s}$, i.e. $\Delta_{\rm s} < \Delta_{\rm p}$. The current reshaper is executed for every time interval $\Delta_{\rm p}$ given the present state $\boldsymbol{x}_k$ at time t_k, as shown by Line 4-7. For every time instance t_i, the input $\boldsymbol{u}_i$ is calculated by

interpolating the reshaped control $\boldsymbol{u}_k$ from (20) with zero-order hold, as indicated in Line 9.

Algorithm 1: Real-time Fast-charging Framework

Input: $k=-1$, $t_{i=0}=0$, $\boldsymbol{x}_0 \coloneqq \boldsymbol{x}(t_0)$, Δ_p, Δ_s, N_p

1 $\hat{\boldsymbol{x}}_{1:N_\mathrm{p}}, \hat{\boldsymbol{u}}_{0:N_\mathrm{p}-1}, \hat{t}_\mathrm{f} \leftarrow$ solve (19) given $\boldsymbol{x}_0$ at time t_0

2 **while** $\mathrm{SoC}_i < \mathrm{SoC}_\mathrm{des}$ **do**

3 observe $\boldsymbol{x}_i$ and T_amb at time t_i

4 **if** $t_i \ \% \ \Delta_\mathrm{p} == 0$ **then** `// for every time interval` Δ_p

5 $k \leftarrow k+1$

6 $\boldsymbol{u}_k \leftarrow$ solve (20) with $\boldsymbol{x}_k, T_\mathrm{amb}$ at time t_k

7 $t_k \leftarrow t_k + \Delta_\mathrm{p}$

8 **else** apply $\boldsymbol{u}_i$ given $\boldsymbol{u}_k$ and zero-order hold

9 $t_i \leftarrow t_i + \Delta_\mathrm{s}$, $i \leftarrow i+1$

IV. Numerical Experiments

This section presents some numerical results to validate the effectiveness of the proposed framework. A comparison study is performed for several strategies. The proposed framework Algorithm 1 is named strategy P1. Two baseline strategies, referred to as B1 and B2, interpolate the reference control trajectory $\hat{\boldsymbol{u}}_{0:N_\mathrm{p}-1}$ given present time t_k as $\tilde{\boldsymbol{u}}_k$ for every time interval Δ_p. Then the interpolated control $\tilde{\boldsymbol{u}}_k$ is passed through a clipping function to ensure that the current at the next time step does not violate the current constraint (17a). This step compensates for quantization errors caused by integrating the fictitious control with differing discretization intervals Δ (from (19)) and Δ_p. Strategy B1 can be summarized as

$$\boldsymbol{u}_k = \max((\overline{I} - I_k)/\Delta_\mathrm{p}, \min(\tilde{\boldsymbol{u}}_k, -I_k/\Delta_\mathrm{p})), \tag{21}$$

which limits the control $\boldsymbol{u}_k$ such that I_{k+1} lies in its bound $[0, \overline{I}]$. In other words, strategy B1 replaces Line 6 of Algorithm 1 by (21). The only difference between B1 and B2 is that B2 includes an additional and typical shutdown protocol: if the terminal voltage $V(t) \geq \overline{V} + 0.001$ V, B2 reduces the charging current to 0 A for the duration of the time interval Δ_p. The subsequent discussion on B1 demonstrates that, without the shutdown protocol in B2, B1 significantly violates the voltage constraint (17a), resulting in faster charging compared to other strategies. However, this result is invalid for real-world applications, as charging the battery beyond the maximum voltage $\overline{V}$ poses significant risks, including thermal runaway, thereby compromising the battery's safe operation. Therefore, the inclusion of this shutdown protocol is crucial for B2. Strategy P2 revises the current reshaper's objective (20a) to minimize the discrepancy between the reference and actual fictitious control, i.e. replacing (20a) by $\|\boldsymbol{u}_k - \hat{\boldsymbol{u}}_k\|_2^2$.

The parameters are: $N_\mathrm{p}=300$, $w_\mathrm{s}=10^{-4}$, $\Delta_\mathrm{p}=0.1$ s, $\Delta_\mathrm{s}=0.05$ s. The initial state $\boldsymbol{x}_0 = \mathrm{col}\{0.2 \times \mathbf{1}_5 \text{ V}, 0.5 \times \mathbf{1}_3 \text{ V}, 45+273.15 \text{ K}, 45+273.15 \text{ K}, 0 \text{ A}\}$. $T_\mathrm{amb} = 45 + 273.15$ K. $\underline{\mathrm{SoC}} = 0\%$, $\overline{\mathrm{SoC}} = 100\%$. $\underline{T}_\mathrm{core} = 273.15$ K, $\overline{T}_\mathrm{core} = 333.15$ K. $\underline{T}_\mathrm{surf} = 243.15$ K, $\overline{T}_\mathrm{surf} = 348.15$ K.

TABLE II
Battery Charging Result

Strategy	Charging Time [s]	Computational Time [ms]
P1	**1279.35**	0.94 ± 0.25
P2	1559.75	0.93 ± 0.14
B1	~~1262.15~~[§]	0.01 ± 0.00
B2	1743.6	0.02 ± 0.00

[§]: strikethrough indicates invalid result due to constraint violation

The true discrete-time system dynamics are obtained by forward propagating the continuous-time dynamics (15) with Runge-Kutta 4th order method, the time step Δ_s, and control under zero-order hold, i.e.

$$\boldsymbol{\theta}_{i,1} = \boldsymbol{f}_\mathrm{c}(\boldsymbol{x}_i, \boldsymbol{u}_i), \ \boldsymbol{\theta}_{i,2} = \boldsymbol{f}_\mathrm{c}(\boldsymbol{x}_i + \frac{\Delta_\mathrm{s}}{2}\boldsymbol{\theta}_{i,1}, \boldsymbol{u}_i)$$
$$\boldsymbol{\theta}_{i,3} = \boldsymbol{f}_\mathrm{c}(\boldsymbol{x}_i + \frac{\Delta_\mathrm{s}}{2}\boldsymbol{\theta}_{i,2}, \boldsymbol{u}_i), \ \boldsymbol{\theta}_{i,4} = \boldsymbol{f}_\mathrm{c}(\boldsymbol{x}_i + \Delta_\mathrm{s}\boldsymbol{\theta}_{i,3}, \boldsymbol{u}_i)$$
$$\boldsymbol{x}_{i+1} = \boldsymbol{x}_i + \frac{\Delta_\mathrm{s}}{6}(\boldsymbol{\theta}_{i,1} + 2\boldsymbol{\theta}_{i,2} + 2\boldsymbol{\theta}_{i,3} + \boldsymbol{\theta}_{i,4}).$$

The trajectory optimization (19) and current reshaper (20) are programmed by Python with CasADi [18], compiled as a C library with a nonlinear programming solver IPOPT [19] with its linear solver MUMPS, and then executed at run-time in Python. All the numerical experiments are performed on a desktop equipped with an Intel® Core™ i7-13700 CPU and 32 GB RAM. The optimal final time obtained from the offline trajectory optimization (19) is $\hat{t}_\mathrm{f} = 1262.20$ s, with the relaxation $\hat{\epsilon}_\mathrm{s} = -1.00 \times 10^{-8}$. The computational time is 0.23 s. The corresponding time step for the optimal reference trajectory $\hat{\boldsymbol{x}}_{1:N_\mathrm{p}}, \hat{\boldsymbol{u}}_{0:N_\mathrm{p}-1}$ is $\Delta = t_\mathrm{f}/N_\mathrm{p} = 4.21$ s. Although this particular computational time seems promising for real-time applications, further reducing the large discretization interval $\Delta = t_\mathrm{f}/N_\mathrm{p}$ would substantially increase the computational burden, primarily due to the curse of dimensionality. The optimal reference trajectory is provided to four strategies: P1, P2, B1, and B2. The numerical experimental results are summarized in Table II.

A. Result Analysis

Fig. 5 illustrates the optimal reference trajectory of terminal voltage and the terminal voltage trajectories under strategies B1 and B2. Although the optimal reference trajectory with a coarse time step does not violate the terminal voltage constraint (17a), the actual terminal voltage trajectory under B1 violates the constraint roughly since 650 s, resulting in the shortest but invalid charging speed in Table II. As illustrated by Fig. 6, to avoid such constraint violation, B2 reduces the charging current to 0 A roughly between 650 s and 1250 s, resulting in a longer charging time.

The proposed strategy P1 charged the battery from 20% SoC to 98% in approximately 21 minutes. Strategy P2, on

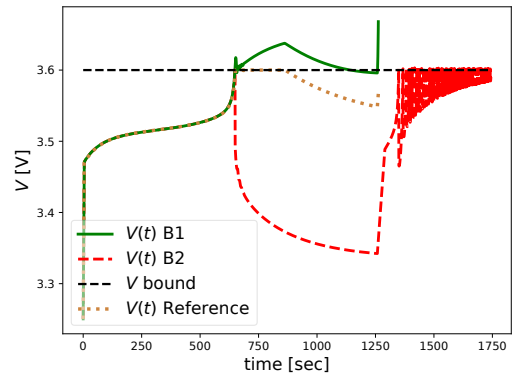

Fig. 5. Terminal voltage trajectories of optimal reference, B1, and B2.

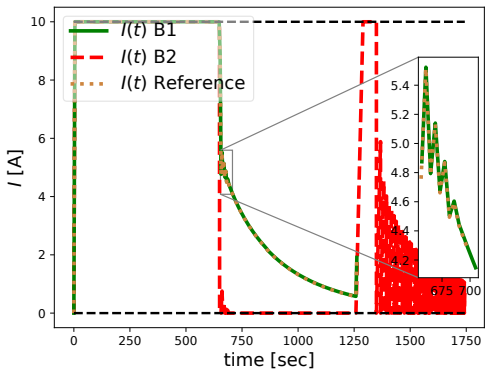

Fig. 6. Charging current trajectories of optimal reference, B1, and B2. Black dashed lines indicate bounds.

the other hand, required approximately 26 minutes to reach $\text{SoC}_{\text{des}} = 98\%$. The longer charging time in P2 is due to the reduction in charging current for minimizing $\|\boldsymbol{u}_k - \hat{\boldsymbol{u}}_k\|_2^2$. This objective function introduces a current tracking error, caused by the fictitious control mismatch given different time discretization between Δ and Δ_{p}. This discrepancy is also illustrated in Fig. 7a, where this error is reflected by the gap between P2's current and the reference. B2 completed the charging roughly 8 minutes longer than P1. As shown in Table II, the computation time for the proposed strategy P1 is about 0.94 ms, without any coding optimization, indicating its good real-time performance.

Fig. 7b illustrates how the proposed current reshaper enforces the critical terminal voltage constraint by adjusting the optimal reference current. After approximately 650 s, although the optimal reference trajectory with $\Delta = t_{\text{f}}/N_{\text{p}} = 4.21$ s predicts the terminal voltage to remain below the upper bound, direct interpolation by B1 causes a constraint violation due to the mismatch between the dynamics used in the trajectory optimization (19) and actual dynamics, as shown in Fig. 5. Fig. 7c demonstrates the SoC trajectories under P1, P2, and B2, where P1 first reached $\text{SoC}_{\text{des}} = 98\%$ roughly in 21 minutes.

Fig. 8 shows the battery dynamics under strategy P1 and B2. For both P1 (top subfigure) and B2 (middle subfigure), roughly starting from 650 s, the Li-ion concentration $V_{\text{s},1}(t)$ at the anode surface reaches its upper bound and penetrates into the inner part of the anode at a slower rate. This fact slows down the charging process, compared to the first phase when $V_{\text{s},1}(t)$ is less than the upper bound 1 V with constant maximum charging current. When the terminal voltage $V(t)$ reaches its upper bound approximately at 650 s, the SoC is closed to 85% and the charging current must decrease. This is because, with the definition of $V(t)$ in (7), the voltage $R_{\text{o,T}}(t)I(t)$ due to file resistance and over-potentials has to be decreased to avoid exceeding the terminal voltage upper bound. Together with the battery core temperature dynamics (4a) and the internal heat generation rate (5), reducing charging current could decrease $T_{\text{core}}(t)$, which subsequently increases $R_{\text{o,T}}(t)$ and $V(t)$. As the SoC approached 100%, the fidelity of the initial optimal reference trajectory decreased due to the battery's highly nonlinear and contradictory dynamics and voltage response during this stage. This phenomenon also explains the significant oscillations observed in the charging current and terminal voltage after approximately 1350 seconds under strategy B2, as illustrated in Fig. 7a and Fig.7b. In contrast, the numerical experimental study confirms that the proposed real-time current reshaper (strategy P1) effectively balances the charging speed (or equivalently, current magnitude) with the voltage constraint satisfaction.

V. Conclusion

This article investigates fast charging strategies for lithium-ion batteries at high C-rates. An electrochemical-thermal-inspired battery model is presented to accurately capture key dynamics. A real-time fast-charging framework is then proposed, consisting of an offline trajectory optimization and an online current reshaping algorithm. First, the offline component solves a time-optimal charging trajectory optimization problem once at the start of the charging process. This generates an optimal reference trajectory for battery states and controls, which is then used by the online reshaper. Second, the online reshaper continually adjusts the reference charging current in real time to enforce charging constraints. Numerical experiments demonstrate the effectiveness and computational efficiency of the proposed framework. Further work may improve the proposed method's robustness against modeling uncertainty and measurement noise.

References

[1] J. B. Goodenough, "Energy storage materials: a perspective," *Energy Storage Materials*, vol. 1, pp. 158–161, 2015.
[2] X.-G. Yang, T. Liu, S. Ge, E. Rountree, and C.-Y. Wang, "Challenges and key requirements of batteries for electric vertical takeoff and landing aircraft," *Joule*, vol. 5, no. 7, pp. 1644–1659, 2021.
[3] M. Doyle, T. F. Fuller, and J. Newman, "Modeling of galvanostatic charge and discharge of the lithium/polymer/insertion cell," *J. Electrochem. Soc.*, vol. 140, no. 6, p. 1526, 1993.
[4] G. Ning and B. N. Popov, "Cycle life modeling of lithium-ion batteries," *J. Electrochem. Soc.*, vol. 151, no. 10, p. A1584, 2004.

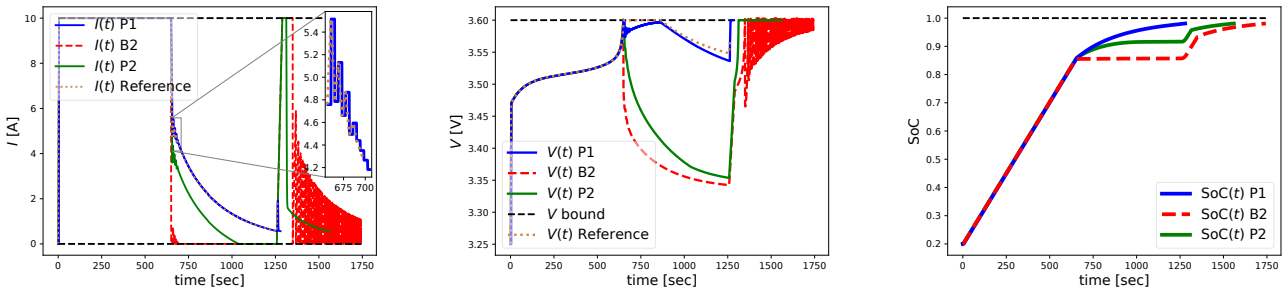

(a) Charging current trajectories of optimal reference, P1, P2, and B2.

(b) Terminal voltage trajectories of optimal reference, P1, P2, and B2.

(c) SoC trajectories of P1, P2, and B2.

Fig. 7. Numerical experimental results of three strategies P1, P2, and B2. Black dashed lines indicate bounds.

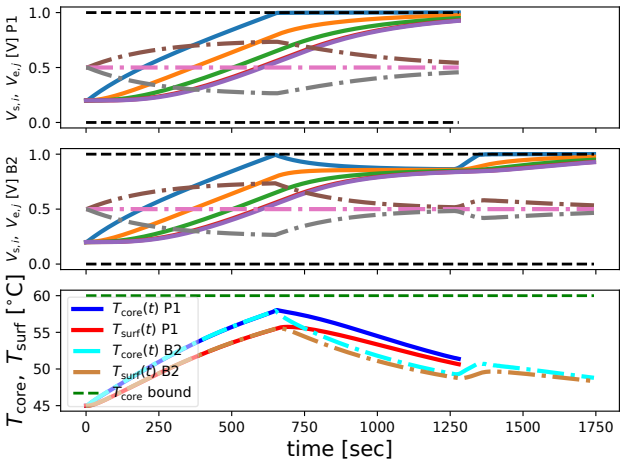

Fig. 8. Trajectories of $V_{\mathrm{s},i}(t)$, $V_{\mathrm{e},j}(t)$ given P1 (top subfigure) and B2 (middle subfigure), and trajectories of $T_{\mathrm{core}}(t)$ and $T_{\mathrm{surf}}(t)$ given P1 and B2. For the top two subfigures, $V_{\mathrm{s},i}$ in solid lines, $i = 1, \cdots, 5$ from left to right; $V_{\mathrm{e},j}$ in dash-dotted lines, $j = 1, 2, 3$ from top to bottom. Black dashed lines indicate bounds for all subfigures.

[5] N. Tian, H. Fang, J. Chen, and Y. Wang, "Nonlinear double-capacitor model for rechargeable batteries: Modeling, identification, and validation," *IEEE Trans. Ctrl. Sys. Tech.*, vol. 29, no. 1, pp. 370–384, 2020.

[6] R. Romagnoli, L. D. Couto, A. Goldar, M. Kinnaert, and E. Garone, "A feedback charge strategy for li-ion battery cells based on reference governor," *Journal of Process Control*, vol. 83, pp. 164–176, 2019.

[7] A. Goldar, R. Romagnoli, L. D. Couto, M. Nicotra, M. Kinnaert, and E. Garone, "Low-complexity fast charging strategies based on explicit reference governors for li-ion battery cells," *IEEE Trans. Ctrl. Sys. Tech.*, vol. 29, no. 4, pp. 1597–1608, 2020.

[8] L. D. Couto, R. Romagnoli, S. Park, D. Zhang, S. J. Moura, M. Kinnaert, and E. Garone, "Faster and healthier charging of lithium-ion batteries via constrained feedback control," *IEEE Trans. Ctrl. Sys. Tech.*, vol. 30, no. 5, pp. 1990–2001, 2021.

[9] S. Feng, R. de Castro, and I. Ebrahimi, "Safe battery control using cascade-control-barrier functions," *IEEE Trans. Ctrl. Sys. Tech.*, 2024.

[10] X. Lin, H. E. Perez, S. Mohan, J. B. Siegel, A. G. Stefanopoulou, Y. Ding, and M. P. Castanier, "A lumped-parameter electro-thermal model for cylindrical batteries," *Journal of Power Sources*, vol. 257, pp. 1–11, 2014.

[11] Y. Li, T. Wik, Y. Huang, and C. Zou, "Nonlinear model inversion-based output tracking control for battery fast charging," *IEEE Trans. Ctrl. Sys. Tech.*, vol. 32, no. 1, pp. 225–240, 2024.

[12] Z. Lu, H. Tu, H. Fang, Y. Wang, and S. Mou, "Integrated optimal fast charging and active thermal management of lithium-ion batteries in extreme ambient temperatures," *IEEE Trans. Ctrl. Sys. Tech.*, vol. 33, no. 2, pp. 714–728, 2025.

[13] N. Biju and H. Fang, "Battx: An equivalent circuit model for lithium-ion batteries over broad current ranges," *Applied Energy*, vol. 339, p. 120905, 2023.

[14] S. J. Moura, F. B. Argomedo, R. Klein, A. Mirtabatabaei, and M. Krstic, "Battery state estimation for a single particle model with electrolyte dynamics," *IEEE Trans. Ctrl. Sys. Tech.*, vol. 25, no. 2, pp. 453–468, 2016.

[15] S. G. Marquis, V. Sulzer, R. Timms, C. P. Please, and S. J. Chapman, "An asymptotic derivation of a single particle model with electrolyte," *J. Electrochem. Soc.*, vol. 166, no. 15, p. A3693, 2019.

[16] R. Mehta and A. Gupta, "An improved single-particle model with electrolyte dynamics for high current applications of lithium-ion cells," *Electrochimica Acta*, vol. 389, p. 138623, 2021.

[17] Z. Geng, J. Groot, and T. Thiringer, "A time-and cost-effective method for entropic coefficient determination of a large commercial battery cell," *IEEE Trans. Transp. Electr.*, vol. 6, no. 1, pp. 257–266, 2020.

[18] J. A. Andersson, J. Gillis, G. Horn, J. B. Rawlings, and M. Diehl, "Casadi: a software framework for nonlinear optimization and optimal control," *Math. Program. Comput.*, vol. 11, pp. 1–36, 2019.

[19] A. Wächter and L. T. Biegler, "On the implementation of an interior-point filter line-search algorithm for large-scale nonlinear programming," *Mathematical Programming*, vol. 106, pp. 25–57, 2006.